# Frequency Characteristics Analysis for Magnetic Anomaly Detection

Jiazeng Wang, Zekun Jiang, Junqi Gao, Shuxiang Zhao, Wenmin Zhai, and Ying Shen, *Member, IEEE*

***Abstract*— This letter presents a frequency characteristics analysis for a magnetic anomaly detection (MAD) study. A magnetic dipole model is developed to study the energy distribution of the obtained MAD signal in the frequency domain, where $f_h$ is proposed to define the signal high-frequency boundary. The relations between $f_h$ and other parameters, such as the velocity of the target (or platform), closest path approach (CPA), magnetic moment strength, magnetic moment orientation (MMO), and sensor orientation, are analyzed. We find that the frequency response is independent of the moment strength. The combined effects of the MMO and sensor orientation on $f_h$ are defined by the functio $ng(\alpha, \beta, \theta, \phi)$, which is studied by the Monte Carlo method, yielding a maximum value of $\max(g) \approx 0.85$. Thus, the function $f_h = 0.85v/\text{CPA}$ is advanced for frequency boundary estimation. The proposed theoretical analysis is examined in an experiment to aid in extracting the magnetic anomaly signal effectively.**

***Index Terms*— Frequency boundary, frequency characteristic, magnetic anomaly detection (MAD).**

## I. Introduction

ANOMALY detection, such as in magnetic and hyperspectral remote sensing [1], [2], is to detect a hidden target whose distinct spacial and spectral information deviate from the background. The geomagnetic field around a ferromagnetic object experiences magnetic disturbances due to its higher permeability than that of most media, including air, soil, water, and sea water. Magnetic anomaly detection (MAD) is a method that detects such magnetic disturbances and mainly focuses on two main categories: target detection and target characteristics analysis. As the magnetic anomaly signal is concentrated in the extreme-low-frequency (ELF) region, it is always submerged in the environmental low-frequency $1/f^{\alpha}$ noise, where $0 < \alpha < 2$ [3]. Therefore, extraction of the weak signal from the background noise is the primary task for any MAD measurements.

For target detection, available noise suppression methods include the classical orthogonal basis functions (OBFs) [4], high-order crossing (HOC) approach [5], and minimum entropy detector (MED) [3], [6]. Being designed for discovering a target, these methods generally result in a filtered signal in the form of a detection probability. Although the signal-to-noise ratio (SNR) is improved, the important magnetic anomaly fingerprint characteristics, such as the wavelet width, shape, and peak values, are undesirably lost.

Target detection has an elementary purpose; however, a comprehensive interpretation of the target characteristics is of critical importance to recognize the features of the cryptic object. Integral magnetic anomaly waveforms are indispensable for characteristics analysis in terms of object localization [7], [8], discrimination [9], [10], trajectory prediction [11], [12], and moment direction estimation [13], [14]. Indeed, it poses great challenges to eliminate the noise and simultaneously preserve the integrity of the signature, which are both located in the ELF region. Therefore, this is possibly the most difficult obstacle for the practical use of the magnetic anomaly signatures.

Various attempts have been made to pick up the weak magnetic anomaly signal of interest. For aeromagnetic detection, the bandpass filter (LPF) frequency was set to 0.06–0.6 Hz [15], [16], 0.06–1.6 Hz [17], and 0.1–0.3 Hz [18]. Vehicle sensing studies have adopted a filtering frequency of 0.001–7 Hz [19] and 0.6–10 Hz [20]. With respect to public safety applications, an access frequency bandwidth of $0.5 < f < 5$ Hz is applied for human-carried suspicious metallic item detection [21]. Therefore, the available LPF selections are very different because researchers selected the filtering frequencies empirically to eliminate the dominant low-frequency background noise at the expense of losing certain signal energies for the purpose of target detection. For advanced sensing purposes of target localization, tracing, and identification, preservation of the entire magnetic signature waveform is an essential prerequisite to employ the waveform extremum, width, and shape [22].

Recent studies have indicated a dependence of the velocity and closest path approach (CPA) on the MAD frequency characteristics [5], [23]. However, with the development of the MAD technique, the platform (or target) has evolved from aircraft for military reconnaissance to cars, surface ships, unmanned underwater vehicles, conveyor belts, and walkers. Among various detection scenarios, there are large differences in the magnetic moment, sensing range, and velocity of the platform (or target). Even the same scenario cannot ensure uniformity in sensing conditions. Moreover, other than the velocity and CPA, the question of whether other factors contribute to the frequency characteristics remains unanswered.

This study reports the achievement of a theoretical and experimental analysis of the dependence of the

Manuscript received December 2, 2020; revised January 15, 2021; accepted January 19, 2021. This work was supported in part by the Academy of Space Electronic Information Technology under Grant 6142411183410 and in part by the Acoustic Science and Technology Laboratory under Grant JCKYS2019604SSJS005 and Grant JCKYS2020604SSJS006. *(Corresponding author: Ying Shen.)*

The authors are with the Acoustic Science and Technology Laboratory, Harbin Engineering University, Harbin 150001, China, also with the Key Laboratory of Marine Information Acquisition and Security, Ministry of Industry and Information Technology, Harbin Engineering University, Harbin 150001, China, and also with the College of Underwater Acoustic Engineering, Harbin Engineering University, Harbin 150001, China (e-mail: shenying@hrbeu.edu.cn).

Color versions of one or more figures in this letter are available at https://doi.org/10.1109/LGRS.2021.3053653.

Digital Object Identifier 10.1109/LGRS.2021.3053653

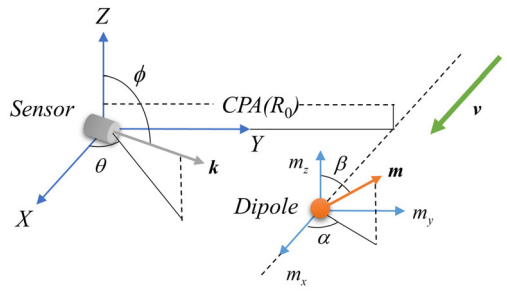


Fig. 1. Schematic of a moving magnetic dipole and a stable sensor.

MAD frequency characteristics on the magnetic moment strength, magnetic moment orientation (MMO), vector sensor orientation, velocity, and CPA. It turns out that (1) the moment strength has no effect on the frequency response; (2) the upper frequency boundary $f_h$ is linearly proportional to the velocity but inversely proportional to the CPA; and (3) a straightforward estimation function $f_h = 0.85\upsilon/\text{CPA}$ is advanced for frequency characteristics analysis and on-site denoising processes. This method is adaptive for various MAD applications, such as intruder detection, intelligent transportation monitoring, sea mine hunting, and so on.

## II. Theoretical Analysis

A magnetic dipole model is established to analyze the induced magnetic anomaly signal and frequency characteristics, given that the dipole model is satisfied.

### A. Theoretical Model

The induced magnetic field $\boldsymbol{B}$ generated by the dipole is expressed as

$$\boldsymbol{B}(\boldsymbol{m},\boldsymbol{r}) = \frac{\mu_0}{4\pi}\left[\frac{3(\boldsymbol{m}\cdot\boldsymbol{r})\boldsymbol{r}}{|\boldsymbol{r}|^5} - \frac{\boldsymbol{m}}{|\boldsymbol{r}|^3}\right] \tag{1}$$

where $\mu_0 = 4\pi \times 10^{-7}$ H/m is the vacuum permeability, $\boldsymbol{r} = [x\,y\,z]^{\mathrm{T}}$ is the dipole position vector, and $\boldsymbol{m} = [m_x m_y m_z]^{\mathrm{T}}$ is the dipole magnetic moment vector.

Fig. 1 shows the detection scheme comprising a vector magnetic sensor and a dipole moving at a constant velocity $\upsilon$. The sensor is assigned at the origin point of the orthogonal coordinate system, where the $xy$-plane is defined by the sensor and the dipole trajectory. The motion direction is along the positive $x$-axis. Angle $\alpha$ is the angle between the positive $x$-axis and the projection of $\boldsymbol{m}$ onto the $xy$-plane, and $\beta$ is the angle between $\boldsymbol{m}$ and the positive $z$-axis. Angle $\theta$ is the angle between the positive $x$-axis and the projection of sensor orientation $\boldsymbol{k}$ onto the $xy$-plane, while $\phi$ is the angle between $\boldsymbol{k}$ and the positive $z$-axis.

Then the position vector at time $t$ can be obtained as

$$x = \upsilon t \quad y = R_0 \quad z = 0. \tag{2}$$

In this model, magnetic moment $\boldsymbol{m}$ can be defined as

$$\boldsymbol{m} = |\boldsymbol{m}|\left[\cos\alpha\sin\beta\ \sin\alpha\sin\beta\ \cos\beta\right]^{\mathrm{T}}. \tag{3}$$

Then the dipole-induced magnetic anomaly signal $\boldsymbol{B}(t)$ can be rewritten as (4), as shown at the bottom of the next page.

The orientation of this vector sensor is denoted by a unit vector $\boldsymbol{k}(\theta,\phi)$ given as

$$\boldsymbol{k}(\theta,\phi) = [\cos\theta\sin\phi\ \sin\theta\sin\phi\ \cos\phi\,]. \tag{5}$$

It can be observed that angles $\alpha$ and $\theta$ both vary in a range of 0°–360°, while angles $\phi$ and $\beta$ are bounded to change within 0°–180°. Thus, the sensor output signal $\boldsymbol{B}_s(t)$ is the projection of the dipole magnetic vector $\boldsymbol{B}(t)$ along the sensor orientation $\boldsymbol{k}$, which can be expressed as

$$\boldsymbol{B}_s(t) = \boldsymbol{k}(\theta,\phi)\cdot\boldsymbol{B}(t). \tag{6}$$

As shown in (4)–(6), the obtained magnetic anomaly signal $\boldsymbol{B}_s(t)$ is dependent on $\alpha$, $\beta$, $\theta$, $\phi$, $R_0$, $\upsilon$, and $|\boldsymbol{m}|$. Next the effect of these parameters on the frequency characteristics of the magnetic anomaly signal will be analyzed.

### B. Frequency Characteristics Analysis

The frequency spectrum of $\boldsymbol{B}_s(t)$ is defined by

$$S(f) = \int_{-\infty}^{+\infty} B_s(t)\cdot e^{-j2\pi ft}dt. \tag{7}$$

We use $f_l$ and $f_h$ as the lower and upper frequency boundaries of the signal energy distribution, respectively. Since the energy of the MAD signal is largely concentrated in an ELF and even quasi-static wideband, the lower frequency limit $f_l$ can be assumed to be zero. The reason for $f_l$ starting from dc ($f_l = 0$) is the nature of MAD, that is, the abnormal phenomenon of a dc Earth magnetic field disturbed by ferromagnetic objects.

Then 99% of the entire signal energy can be obtained by

$$\exists f_h : \int_0^{f_h}(S(f))^2df = 0.99\int_0^{\infty}(S(f))^2df \tag{8}$$

where $f_h$ can be regarded as the upper side frequency covering 99% of the signal energy. Equations (4)–(8) clearly suggest that $f_h$ is dependent on $|\boldsymbol{m}|$, MMO($\alpha$, $\beta$), $\boldsymbol{k}(\theta,\phi)$, $R_0$, and $\upsilon$.

Next the control variable method is used to study the effects of each variable on $f_h$ under the conditions of $|\boldsymbol{m}| = 2$ A·m$^2$, $R_0 = 1.2$ m, $\upsilon = 0.8$ m/s, MMO $(\alpha, \beta) = (143°, 72°)$, and $\boldsymbol{k}(\theta, \phi) = (115°, 28°)$. It should be noted that seven variables are arbitrarily selected, producing characteristic correlation curves or contour diagrams as shown in Fig. 2.

The effect of the moment strength is first examined at fixed $R_0 = 1.2$ m, $\upsilon = 0.8$ m/s, MMO $(\alpha, \beta) = (143°, 72°)$, and $\boldsymbol{k}(\theta, \phi) = (115°, 28°)$ while $|\boldsymbol{m}|$ changes from 1 to 20 A·m$^2$. The induced $f_h$ curve as a function of $|\boldsymbol{m}|$ is presented in Fig. 2(a), showing that $f_h$ is independent of $|\boldsymbol{m}|$. In contrast, $f_h$ is linearly dependent on both $R_0$ and $\upsilon$, as illustrated in Fig. 2(b). Furthermore, the results also imply that $f_h$ is proportional to $\upsilon$ but inversely proportional to $R_0$. However, the influences of MMO $(\alpha, \beta)$ and $\boldsymbol{k}(\theta, \phi)$ on $f_h$ are nonlinear, as shown in Fig. 2(c) and (d), respectively. Thus, this leads to rewriting $f_h$ in the following form:

$$f_h = \frac{\upsilon}{R_0}\cdot g(\alpha,\beta,\theta,\phi) \tag{9}$$

where $g$ is a function of angles $\alpha$, $\beta$, $\theta$, and $\phi$. The intended use of (9) is to estimate the highest frequency boundary by identifying the extremum values of the $R_0$, $\upsilon$, and $g$ functions.

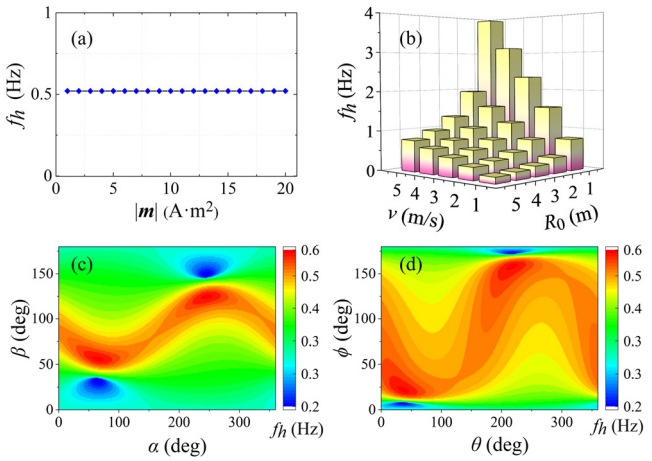


Fig. 2. Effects of different parameters on $f_h$: (a) effect of magnetic moment magnitude $|\boldsymbol{m}|$. (b) Effects of $v$ and CPA. (c) Effect of $\boldsymbol{m}'(\alpha, \beta)$. (d) Effect of $\boldsymbol{k}(\theta, \phi)$.

Please note that the specific mathematical expression of $g(\alpha, \beta, \theta, \phi)$ is difficult to obtain. To estimate the ceiling value of the $g$ function, our analysis method follows classical statistical signal processing techniques based on Monte Carlo simulation [24]. The Monte Carlo method is valid for finding suboptimal approximations with the likelihood of using little work, eliminating the need for a more complicated computation.

A schematic flowchart of obtaining function $g$ by Monte Carlo simulation is illustrated in Fig. 3, which comprises two steps. First, a number of generator is used to randomly produce variables $(\alpha, \beta, \theta, \phi)$ under the conditions of $\alpha, \theta \in (0^\circ\ 360^\circ)$, and $\beta, \phi \in (0^\circ\ 180^\circ)$, which is employed in dipole model (4)–(6). As $\boldsymbol{B}_s(t)$ is dependent on $\alpha$, $\beta$, $\theta$, $\phi$, $R_0$, $v$, and $|\boldsymbol{m}|$, constant values of $R_0$, $v$, and $|\boldsymbol{m}|$ are assigned to (6), which can be set as any value. The second step is to compute the signal spectrum $S(f)$ with (7) and the upper frequency boundary $f_h$ based on (8). By assigning $R_0$ and $v$ for (9), a unique value of $g$ is developed due to the available value of $f_h$. Note that a $g$ value is developed during each simulation loop by randomly selecting variables $(\alpha, \beta, \theta, \phi)$. The simulation was carried out by randomly selecting $10^6$ groups of uniformly distributed $\alpha$, $\beta$, $\theta$, and $\phi$ with $\alpha$ and $\theta$ in the range of $(0^\circ\ 360^\circ)$ and $\beta$ and $\phi$ in $(0^\circ\ 180^\circ)$. After $10^6$ computations, the probability distribution of $g$ in a characteristic range of $0.270 \le g \le 0.852$ is obtained.

Then (9) can be obtained as follows:

$$f_h \approx 0.85 \cdot \frac{v}{R_0}. \tag{10}$$

Equation (10) suggests that $f_h$ is only dependent on $R_0$ and $v$. To this end, searching for the largest value of $f_h$ turns into determining the limits of $R_0$ and $v$.

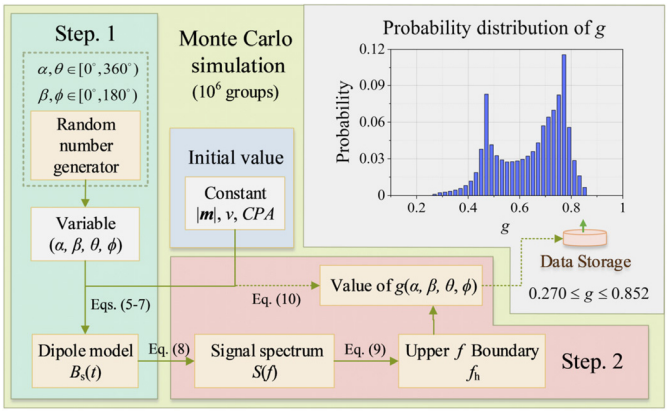


Fig. 3. Schematic flowchart of obtaining function $g$ by Monte Carlo simulation.

Indeed, with respect to the different detection scenarios, it is likely that the extremums for $R_0$ and $v$ are recognized in advance. For example, in aeromagnetic remote sensing, $R_0$ and $v$ usually have very large spans of $100 \le R_0 \le 1000$ m and $50 \le v \le 300$ m/s, respectively, producing a characteristic distribution of $f_h$. This corresponds to a smallest value of $f_h = 0.04$ Hz when $(R_0, v) = (1000, 50)$ and a largest value of $f_h = 2.6$ Hz when $(R_0, v) = (100, 300)$. The estimated interval of $0.04 \le f_h \le 2.6$ Hz can be taken as the frequency distribution characteristics for aeromagnetic detection in the typical sensing conditions, as shown in Fig. 4.

By updating parameters $R_0$ and $v$ specifically, this estimation method for $f_h$ is adaptable to other kinds of detection scenarios, such as surface ship, car detection, and indoor tests. To summarize, a schematic chart of $f_h$ for comprehensive cases is presented in Fig. 4. It shows that different MAD applications manifest themselves in identifiable $f_h$ distributions in the ranges of $0.04 \le f_h \le 2.6$ Hz for aeromagnetic detection, $0.0017 \le f_h \le 0.26$ Hz for surface ship detection, $0.04 \le f_h \le 4.3$ Hz for car detection, and $0.04 \le f_h \le 21.3$ Hz for indoor applications. This knowledge of MAD frequency characteristics allows substantial advances in the extraction of the target signal for optimal filtering, even if very little information about the target and sensor is provided.

## III. Experimental Verification

The option to explore (10) opens the possibility of using such a magnetic anomaly characteristics frequency boundary to accurately extract the target signal seriously blurred by external noise. This argument is exemplified in the case of identifying the optimal cutoff frequency ($f_c$) by $f_c = f_h$ for an LPF to recover the featured signal. In other words, an LPF with $f_c = f_h$ should cover almost the entire signal energy with a relatively high SNR.

$$\boldsymbol{B}(t) = \frac{\mu_0 |\boldsymbol{m}|}{4\pi R_0^3} \begin{bmatrix} \dfrac{2(vt/R_0)^2 - 1}{(1 + (vt/R_0)^2)^{5/2}} & \dfrac{3(vt/R_0)}{(1 + (vt/R_0)^2)^{5/2}} & 0 \\ \dfrac{3(vt/R_0)}{(1 + (vt/R_0)^2)^{5/2}} & \dfrac{2 - (vt/R_0)^2}{(1 + (vt/R_0)^2)^{5/2}} & 0 \\ 0 & 0 & \dfrac{-(vt/R_0)^2 - 1}{(1 + (vt/R_0)^2)^{5/2}} \end{bmatrix} \boldsymbol{m}' \tag{4}$$

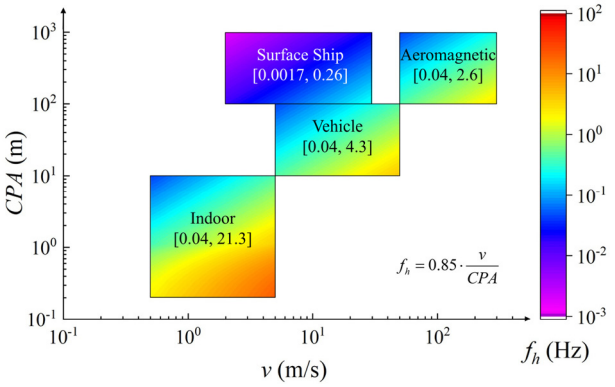


Fig. 4. $f_h$ (Hz) distribution diagram of the MAD signal in different detection scenarios.


Fig. 5. Photograph of the (a) vehicle experiment. (b) surface ship experiment.

### A. Experimental Setup

Ground and marine vehicle experiments were performed as shown in Fig. 5(a) and (b), respectively. The detection device was based on a fluxgate magnetometer with a sensitivity of 10 V/Oe and a self-noise of 25 pT/$\sqrt{}$Hz at $f = 1$ Hz.

Vehicle detection was performed at Qingdao, Shandong Province (N35°47', E120°02'). The vehicle, a standard one-ton sedan with a length of 4 m, passed by the magnetometer at $v = 40$ km/h (11.1 m/s) in the east to west direction with CPA = 20 m. Detection for a 60-ton, 29.5-m long and 6.2-m wide vessel was conducted at N35°44', E120°10', a sea area near Lingshan Island of Qingdao. The ship was sailing from south to north at $v = 10$ Kn (5.1 m/s) and around CPA = 125 m. Note that the magnetic field induced by the moving target can only be taken with good approximation as a dipole when the CPA is beyond 3–5 times the length of the target.

### B. Experimental Results

For the vehicle detection, the obtained raw signal is shown in Fig. 6(a) at a sampling frequency of $f_s = 50$ Hz. Due to the poor SNR, the noise leaves ambiguity in the waveform features, such as the waveform width and peak value, which are essential parameters to predict the target behavior. The signal high-frequency boundary is calculated to be $f_h = 0.47$ Hz, when $v = 11.1$ m/s and CPA = 20 m according to (10). To extract the magnetic anomaly signal, $f_c = f_h = 0.47$ Hz is chosen to perform LPF signal processing, as shown in Fig. 6(b). Clearly, the filtered signal results in good denoising performance and complete signal extraction. Fig. 6(c) shows the corresponding raw anomaly

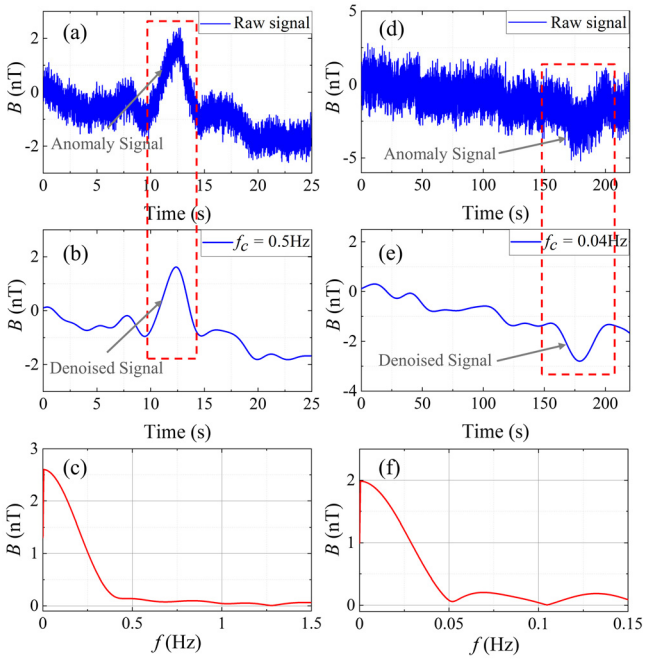


Fig. 6. (a) Raw signal with $f_s = 50$ Hz in vehicle MAD. (b) LPF processing with $f_c = 0.47$ Hz in vehicle MAD. (c) Raw anomaly signal spectrum in vehicle MAD. (d) Raw signal with $f_s = 50$ Hz in ship MAD. (e) LPF processing with $f_c = 0.035$ Hz in ship MAD. (f) Raw anomaly signal spectrum in ship MAD.

signal spectra, which refers to the time-domain signal within the dashed lines in Fig. 6(a). We can see that the signal energy dominates in $f \leq 0.47$ Hz and attenuates quickly to null with increasing frequency.

The ship MAD signal is also seriously corrupted by the background noise, as illustrated in Fig. 6(d), making it difficult to distinguish. Equation (10) yields $f_h = 0.035$ Hz under the conditions of $v = 5$ m/s and CPA = 125 m. The LPF performance is then conducted by setting $f_c = f_h = 0.035$ Hz. One can see that the use of the LPF leads to good signal recovery and noise depression simultaneously, as depicted in Fig. 6(e). The corresponding raw anomaly signal spectra is illustrated in Fig. 6(f), implying that the ship-induced signal energy is largely less than 0.05 Hz. It matches well with the predicted $f_h = 0.035$ Hz. The spectra data shown in Fig. 6(c) and (f) both verify the effectiveness of the proposed frequency characteristics analysis method.

We can see that the desirable $f_c$ differs in car and ship detections. This is due to the different target moving velocities and CPAs that combine together to govern the characteristic $f_h$. While the experiments have not allowed for comprehensive examination of all the detection settings illustrated in Fig. 4, we believe that the theoretical prediction of $f_h$ is physically correct. Thus, engineers can readily identify a reasonable $f_c$ for target signal pick up according to the predictable velocity and CPA ranges in specific detection settings.

## IV. Discussion

To evaluate the effect of the accurate determination for $f_h$, the algorithm is examined for our recent study [11] for dipole MMO estimation. In the simulation, the target magnetic moment strength is set to be $|\boldsymbol{m}| = 1$ A·m$^2$ and MMO($\alpha$, $\beta$) = (20°, 153°). The target is moving along the $x$-axis at

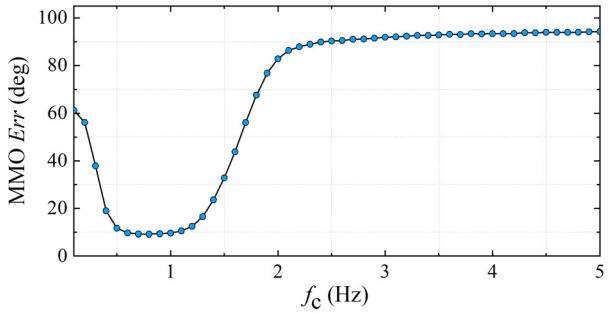


Fig. 7. MMO Estimation error *Err* as a function of $f_c$.

velocity of $\upsilon = 1$ m/s and CPA = 1 m. Gaussian white noise is added to mimic the high-frequency noise nuisance from environment, and the mixed signal is processed by an LPF with different $f_c$ to reject the noise. The obtained filtered signal is then employed for target MMO estimation. In order to evaluate the filtering effect by means of $f_c$, the estimated MMO error Err $= [(\alpha - \alpha_e)^2 + (\beta - \beta_e)^2]^{1/2}$ is used, where $(\alpha, \beta)$ is the actual MMO and $(\alpha_e, \beta_e)$ is the estimated one. The average *Err* is calculated by $10^4$ groups of Monte Carlo computation, and the simulation results are shown in Fig. 7.

The simulation data indicates that *Err* can achieve a minimum error value of around 8° for $0.6 < f_c < 1$ Hz. It can also be seen that Err increases rapidly to 80° as the $f_c$ was increased to 2 Hz. The accurate prediction for MMO is directly dependent on the careful selection of the $f_c$ to depress the high-frequency interferences.

According to (10), the ideal cutoff frequency for the LPF is $f_c = f_h = 0.85$ Hz, which can be seen to agree well with the simulation results. Such frequency distribution characteristics analysis for dipole incurred magnetic anomaly signal offers a new MAD technology that is promising for use in magnetic anomaly signature extraction to estimate the MMO.

## V. Conclusion

In summary, the frequency distribution characteristics of magnetic anomaly signals are investigated. Theoretical analysis indicates that the upper frequency boundary $f_h$ of the MAD signal energy is dependent on the velocity $\upsilon$, CPA, magnetic moment direction MMO $(\alpha, \beta)$, and sensor orientation $\boldsymbol{k}(\theta, \phi)$ but independent of the magnetic moment strength $|\boldsymbol{m}|$. Furthermore, $f_h$ is found to be linearly dependent on both $\upsilon$ and CPA. The combination of angles $\alpha$, $\beta$, $\theta$, and $\phi$ is grouped into a function $g(\alpha, \beta, \theta, \phi)$, which has been recognized to have the largest value of $\max(g) \approx 0.85$ by the Monte Carlo method. Then $\upsilon$ and CPA are used as essential cues to define $f_h$ with a transfer function of $f_h = 0.85\upsilon$/CPA. This argument is demonstrated by experiments in the vehicle and vessel detections.

The merit of the $f_h$ estimation function is essential for not only comprehending the MAD signal frequency responses but also extracting the ELF region. The proposed frequency characteristic function $f_h = 0.85\upsilon$/CPA directs us in how to identify the frequency boundary of the signal of interest according to the possible $\upsilon$ and CPA limit values.

## References

[1] Y. Yuan, D. Ma, and Q. Wang, "Hyperspectral anomaly detection by graph pixel selection," *IEEE Trans. Cybern.*, vol. 46, no. 12, pp. 3123–3134, Dec. 2016.

[2] Y. Yuan, D. Wang, and Q. Wang, "Anomaly detection in traffic scenes via spatial-aware motion reconstruction," *IEEE Trans. Intell. Transp. Syst.*, vol. 18, no. 5, pp. 1198–1209, May 2017.

[3] Y. Tang *et al.*, "Detection of magnetic anomaly signal based on information entropy of differential signal," *IEEE Geosci. Remote Sens. Lett.*, vol. 15, no. 4, pp. 512–516, Apr. 2018.

[4] B. Ginzburg, L. Frumkis, and B.-Z. Kaplan, "Processing of magnetic scalar gradiometer signals using orthonormalized functions," *Sens. Actuators A, Phys.*, vol. 102, nos. 1–2, pp. 67–75, Dec. 2002.

[5] A. Sheinker, B. Ginzburg, N. Salomonski, P. A. Dickstein, L. Frumkis, and B.-Z. Kaplan, "Magnetic anomaly detection using high-order crossing method," *IEEE Trans. Geosci. Remote Sens.*, vol. 50, no. 4, pp. 1095–1103, Apr. 2012.

[6] A. Sheinker, N. Salomonski, B. Ginzburg, L. Frumkis, and B.-Z. Kaplan, "Magnetic anomaly detection using entropy filter," *Meas. Sci. Technol.*, vol. 19, no. 4, Apr. 2008, Art. no. 045205.

[7] Y. Shen *et al.*, "AC magnetic dipole localization by a magneto-electric sensor," *Smart Mater. Struct.*, vol. 21, no. 6, Jun. 2012, Art. no. 065007.

[8] J. T. Sherman, J. K. Lubkert, R. S. Popovic, and M. R. DiSilvestro, "Characterization of a novel magnetic tracking system," *IEEE Trans. Magn.*, vol. 43, no. 6, pp. 2725–2727, Jun. 2007.

[9] Y. Ege *et al.*, "A magnetic measurement system and identification method for buried magnetic materials within wet and dry soils," *IEEE Trans. Geosci. Remote Sens.*, vol. 54, no. 3, pp. 1803–1811, Mar. 2016.

[10] S. D. Billings, "Discrimination and classification of buried unexploded ordnance using magnetometry," *IEEE Trans. Geosci. Remote Sens.*, vol. 42, no. 6, pp. 1241–1251, Jun. 2004.

[11] Y. Ege, O. Kalender, and S. Nazlibilek, "Direction finding of moving ferromagnetic objects inside water by magnetic anomaly," *Sens. Actuators A, Phys.*, vol. 147, no. 1, pp. 52–59, Sep. 2008.

[12] Q. Zhou, G. Tong, B. Li, and X. Yuan, "A practicable method for ferromagnetic object moving direction identification," *IEEE Trans. Magn.*, vol. 48, no. 8, pp. 2340–2345, Aug. 2012.

[13] J. Wang, Y. Shen, R. Zhao, C. Zhou, and J. Gao, "Estimation of dipole magnetic moment orientation based on magnetic signature waveform analysis by a magnetic sensor," *J. Magn. Magn. Mater.*, vol. 505, Jul. 2020, Art. no. 166761.

[14] V. Sanchez, Y. Li, M. N. Nabighian, and D. L. Wright, "Numerical modeling of higher order magnetic moments in UXO discrimination," *IEEE Trans. Geosci. Remote Sens.*, vol. 46, no. 9, pp. 2568–2583, Sep. 2008.

[15] M. Hirota *et al.*, "Magnetic detection of a surface ship by an airborne LTS SQUID MAD," *IEEE Trans. Appl. Supercond.*, vol. 11, no. 1, pp. 884–887, Mar. 2001.

[16] T. Inaba, A. Shima, M. Konishi, H. Yanagisawa, J.-I. Takada, and K. Araki, "Magnetic dipole signal detection and localization using subspace method," *Electron. Commun. Jpn.*, vol. 85, no. 5, pp. 23–24, 2002.

[17] C. D. Hardwick, "Important design considerations for inboard airborne magnetic gradiometers," *Geophysics*, vol. 49, no. 11, pp. 2004–2018, Nov. 1984.

[18] X. Zheng *et al.*, "An orthonormalized basis function algorithm based on wavelet analysis for magnetic anomaly detection," presented at the 10th Int. Congr. Image Signal Process., Biomed. Eng. Inform., 2017.

[19] D. Liu *et al.*, "Adaptive cancellation of geomagnetic background noise for magnetic anomaly detection using coherence," *Meas. Sci. Technol.*, vol. 26, no. 1, Jan. 2015, Art. no. 015008.

[20] Y. Shen *et al.*, "Investigation of vehicle induced magnetic anomaly by triple-axis magnetoelectric sensors," *Smart Mater. Struct.*, vol. 21, no. 11, Nov. 2012, Art. no. 115007.

[21] J. Gao, J. Wang, L. Zhang, Q. Yu, Y. Huang, and Y. Shen, "Magnetic signature analysis for smart security system based on TMR magnetic sensor array," *IEEE Sensors J.*, vol. 19, no. 8, pp. 3149–3155, Apr. 2019.

[22] Y. Shen, J. Wang, J. Shi, S. Zhao, and J. Gao, "Interpretation of signature waveform characteristics for magnetic anomaly detection using tunneling magnetoresistive sensor," *J. Magn. Magn. Mater.*, vol. 484, pp. 164–171, Aug. 2019.

[23] Z. Guanyi, Q. Han, X. Tong, and H. Guo, "Adaptive filtering method for magnetic anomaly detection," *J. Appl. Remote Sens.*, vol. 12, no. 2, pp. 1–10, 2018.

[24] S. M. Kay, *Fundamentals of Statistical Signal Processing: Estimation Theory*, vol. 1. Upper Saddle River, NJ, USA: Prentice-Hall, 1993, p. 595.